Effect of pressure on the transport properties and thermoelectric performance of Dirac semimetal $ZrTe_5$

Sanskar Mishra,[1] Nagendra Singh,[1] V. K. Gangwar,[2] Rajan Walia,[3] Manindra Kumar,[1] Udai Bhan Singh,[1] Deepash Sekhar Saini,[1] Jianping Sun,[4] Genfu Chen,[4] Dilip Bhoi,[5] Sandip Chatterjee,[6] Yoshiya Uwatoko,[5] Jinguang Cheng,[4,*] and Prashant Shahi[1,†]

[1]*Department of Physics, DDU Gorakhpur University, Gorakhpur 273009, India*
[2]*Department of Physics, K.G.K. (P.G.) College, Moradabad 244001, India*
[3]*Department of Physics, University of Allahabad, Prayagraj 211002, India*
[4]*Beijing National Laboratory for Condensed Matter Physics and Institute of Physics, Chinese Academy of Sciences, Beijing 100190, China*
[5]*Institute for Solid State Physics, University of Tokyo, Kashiwa, Chiba 277–8581, Japan*
[6]*Department of Physics, Indian institute of technology (IIT)-BHU, Varanasi 221005, India*

(Received 11 April 2025; revised 8 September 2025; accepted 2 October 2025; published 27 October 2025)

$ZrTe_5$ has been extensively studied because of its novel topological properties, which are tunable by subjecting to various parameters like temperature, chemical synthesis conditions, and pressure. In this study, we have investigated and compared the effect of hydrostatic pressure up to ∼20 kbar on the transport properties of $ZrTe_5$ single crystals grown by chemical vapor transport (CVT) and flux methods. With the application of pressure, the electrical resistivity $\rho(T)$ and thermopower $S(T)$ of both crystals were found to increase in the whole temperature range unlike the other known thermoelectric materials, such as Bi_2Te_3, SnSe etc. This observation is supported by complementary first-principles band-structure calculations, as the application of pressure widens the direct band gap at Γ point. Moreover, the analysis of the pressure-dependent magnetotransport and Shubnikov-de Hass oscillation results revealed an increase in carrier concentration and effective mass along with reduction of mobility as pressure rises. Furthermore, with the application of pressure, the flux-grown $ZrTe_5$ crystals display a transition from unipolar to bipolar charge transport as evidenced by the emergence of a resistivity peak at T^* under high pressure, unlike the CVT-grown $ZrTe_5$ crystals where the bipolar charge transport near its characteristic resistivity peak (T_p) remains unaffected. Our study also reveals a pressure-induced enhancement of T_p and T^* for both crystals, suggesting an upward shift of the Fermi level upon compression. Additionally, for the CVT-grown $ZrTe_5$ crystals, the application of pressure nearly doubled the thermoelectric power factor (PF) at 18.2 kbar and room temperature. In contrast, for the flux-grown $ZrTe_5$ crystals, the PF varies weakly as the pressure is raised to 17 kbar. Our results underscore the role of crystal synthesis technique along with the application of pressure as an effective strategy to optimize the magnetotransport and thermoelectric performance of $ZrTe_5$.

DOI: 10.1103/53lr-gc9w

I. INTRODUCTION

$ZrTe_5$, a 2D layered material with relatively weak interlayer bonding (∼12 meV/Å^2), [1] has been studied for a long time because of its anomalous transport properties [2–7]. This material is widely recognized because of a Lifshitz transition [8] at a characteristic temperature (T_p), as evidenced by a characteristic peak in resistivity, sign reversal of the Seebeck coefficient and Hall resistivity [3]. Angle-resolved photoemission spectroscopy (ARPES) studies revealed the shift of the chemical potential across the band gap from hole-like bands to electron-like bands across T_p as temperature is lowered from room temperature [9]. More interestingly, several works [10,11] demonstrated that the shift in chemical potential is sensitively affected by the Te concentration in $ZrTe_5$, resulting in a variation of T_p as well as the transport properties. Therefore, it is likely that the samples used by different groups have different stoichiometric proportions of Te [11]. This is evident from the difference in the transport properties between the crystals grown by chemical vapor transport (CVT) and flux-grown methods. For the CVT-grown crystals, the T_p tends to be higher and varies between ∼130–150 K [12–15], whereas the flux-grown crystals usually display T_p lower than ∼60 K [9,15–17]. In addition, depending on the band shift [12], the anomalous Hall effect (AHE) and chiral magnetic effect are reported in $ZrTe_5$ crystals synthesized by the flux-growth method [18,19]. Previously [10], we have investigated the ambient pressure properties of both CVT, and flux crystals based on a magnetotransport study in which CVT crystals exhibited the bipolar conduction (i.e., simultaneous participation of electrons and holes in conduction), while the flux crystals display unipolar transport where the conduction is dominated solely by hole carriers.

*Contact author: jgcheng@iphy.ac.cn
†Contact author: prashant.phy@ddugu.ac.in

Besides Te vacancies, the physical properties and the Fermi surface topology of $ZrTe_5$ also vary sensitively with the application of pressure [17,20–22]. Zhou *et al.* reported a complete suppression of resistivity peak in $ZrTe_5$ around 6.2 GPa along with the emergence of superconductivity below a transition temperature $T_c \sim 2.0$ K, which is found to increase with pressure, reaching as high as ∼6 K at 21.2 GPa [23]. Similar results related to pressure-induced superconductivity have also been reported in $HfTe_5$ [24], Investigations in the low-pressure regime below 2 GPa revealed more interesting results, including pressure-induced topological phase transitions and changes in Fermi surface topology. J. L. Zhang *et al.* reported a nontrivial to trivial Berry phase shift around ∼2 GPa in the CVT-grown $ZrTe_5$ crystals along with the large suppression of magnetoresistance (MR) as pressure is applied. This has been attributed to the pressure-induced change in the Dirac fermion state near the Fermi level [25]. First-principles calculations under pressure reveals a transition from strong to weak topological insulator phase mediated by an intermediate Dirac semimetallic phase [25]. D. Santos-Cottin *et al.* [26] measured the transport and optical properties of both the CVT and flux-grown crystals. In contrast to the behavior reported in Ref. [27], T_p was found to increase with pressure. On the other hand, T_p in a-few-layer-thick $ZrTe_5$ nanoflakes does not change with pressure [20]. Similarly, T_p of the sister compound $HfTe_5$ almost remains flat up to 1.0 GPa and thereafter keeps decreasing [22]. These results suggest that the variation of T_p that depends on the sample synthesis conditions and varies differently with the application of pressure, remains poorly understood in a unified picture.

Therefore, in this study, we investigated the physical properties of $ZrTe_5$ single crystals under hydrostatic pressures ($0 \leqslant P \leqslant 20$ kbar) using magnetotransport, thermopower (S), and complementary band-structure calculations. A comparison between the $ZrTe_5$ single crystals synthesized by CVT and flux-growth techniques revealed a huge difference in the pressure-induced transport properties. In addition, we observed that both resistivity (ρ) and S increase with increasing pressure, irrespective of the crystal growth techniques, suggesting an unconventional nature compared to other layered thermoelectric materials [28–30]. Notably, the resistivity peak at both T_p and T^* (resistivity peak temperature in the flux sample is denoted by T^* hereafter) of both crystals displays a dramatic variation with pressure. In the CVT crystals, T_p increases up to 155 K around 13 kbar and is followed by a slight decrease upon further increasing pressure. In contrast, a peak-like feature at T^* emerges in $\rho(T)$ of flux-grown crystals with a moderate application of pressure ∼6 kbar and gradually shifts towards higher temperatures. The pressure-induced appearance of T^* in flux crystals mirrors the behavior of CVT crystals (as it already exhibits T_p), therefore it is worth noting that the Te vacancies in CVT Crystals may act as a form of chemical pressure, which refers to lattice compression caused by atomic substitution or vacancies [31]. Hall resistivity $\rho_{xy}(B)$ under pressure of CVT samples is qualitatively the same as that of the ambient pressure, while there is a deviation for the flux samples. At low temperatures, the CVT crystals display a very pronounced quantum (SdH) oscillation at ambient and high pressures, whereas no such features could be observed for the flux crystals. Analyses of magnetotransport behavior under pressure revealed an increase in overall carrier density and effective mass with a concurrent decrease of carrier mobility for both crystals. Furthermore, band-structure calculations reveal the Dirac-like band structure near the Fermi level at ambient pressure, as pressure increases the band gap also increases. In addition, we observed a pressure-induced enhancement in thermoelectric power factor ($PF = S^2/\rho$). Our results suggest that pressure application is an effective strategy to optimize PF and identify $ZrTe_5$ as a promising candidate for energy conversion technology.

II. EXPERIMENTAL AND COMPUTATIONAL DETAILS

The $ZrTe_5$ single crystals were grown by the CVT and flux-growth method as described in Refs. [32,33]. Details about the characterizations of these single crystals have been reported in our previous study [10]. Resistivity was measured using a conventional four-probe method, with the current flowing along the longest direction of the crystal, i.e., the a axis. The temperature-dependent $S(T)$ at ambient and high pressures was measured using a homemade setup (described in an earlier work of our group [30]) integrated with a self-clamped piston-cylinder cell (PCC). For the $S(T)$ measurements, the temperature gradient of $\Delta T/T \sim 1\%$ was maintained along the a axis with the help of a thin-film heater (resistance ∼120 Ω). A AuFe/Chromel differential thermocouple was used to measure the temperature difference (ΔT) with a precision of ∼0.2%. The maximum error in the measurement of $S(T)$ is ∼0.5 μV/K. For high-pressure measurements, Daphne 7373 was used as the pressure transmitting medium. A manganin wire resistance gauge was used to probe the pressure inside the pressure cell. For MR and Hall resistance measurements, a cubic anvil high-pressure cell was used, in which the current was injected along the a axis and the magnetic field was applied along the b axis.

The density functional theory calculations for the structural optimizations, density of states (DOS), and electronic band structure were performed using the Quantum ESPRESSO package [34]. Exchange-correlation effects were treated with the generalized gradient approximation (GGA) using the Perdew-Burke-Ernzerhof (PBE) functional [35] along with Grimme's D3 dispersion corrections for van der Waals interactions [36]. The force and total energy convergence thresholds were set to 10^{-5} atomic units and 10^{-12} Ry, respectively, with a wavefunction (WFC) cut off of Ry. Structural optimizations were performed at both ambient and high-pressure conditions using a pressure-convergence threshold of 0.05 kbar. For these calculations, scalar-relativistic ultra-soft pseudopotentials were employed. DOS and band-structure calculations were performed using fully relativistic pseudopotentials from the PSLibrary [37], taking spin-orbit coupling (SOC) into account. For the band-structure calculations, $15 \times 15 \times 4$ k-point mesh was used, and a denser k-point grid (double that of the original mesh) was applied for the non-self-consistent field DOS calculations to accurately map the Fermi level.

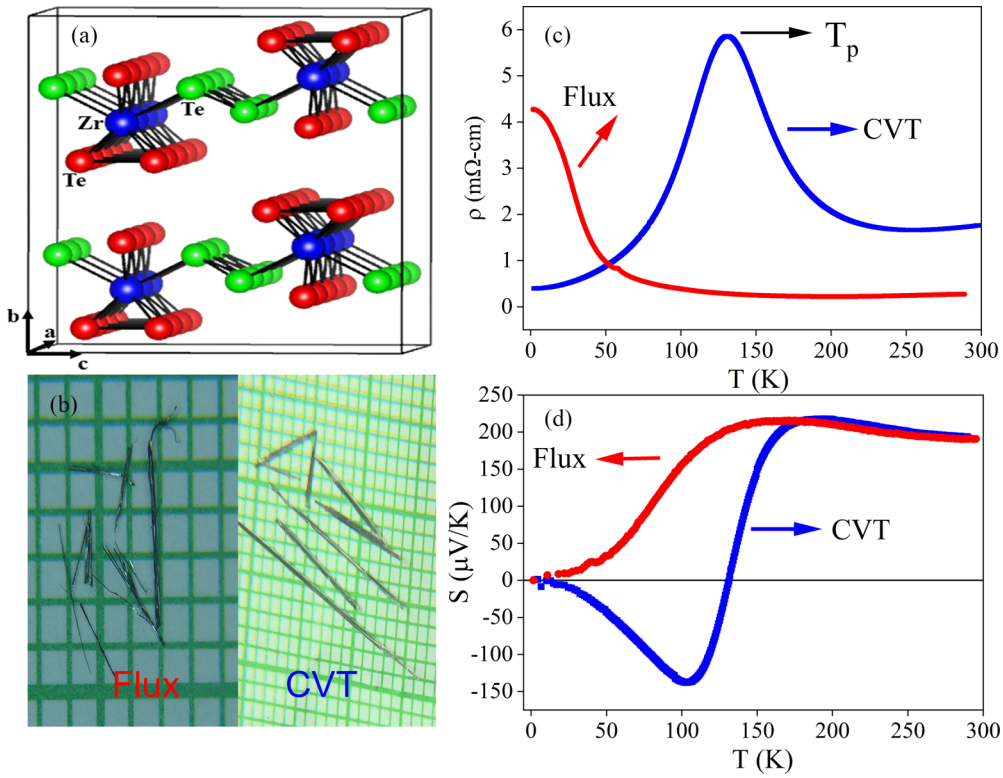

FIG. 1. (a) Crystal structure of $ZrTe_5$, in which the trigonal prismatic chains of $ZrTe_3$ are running along the a axis and two chains are connected by zigzag Te atoms. Two-dimensional layers of $ZrTe_5$ are stacked along the b axis. (b) CVT and flux-grown single crystals of $ZrTe_5$ with the longest dimension up to ∼5 mm. (c), (d) Temperature dependence of a-axis resistivity $\rho(T)$ and thermopower $S(T)$ of $ZrTe_5$ crystals grown by the CVT and flux-grown method.

III. RESULTS

A. Transport properties at ambient pressure

$ZrTe_5$ crystallizes in an orthorhombic layered crystal structure with space group *Cmcm*. Figure 1(a) depicts the crystal structure of $ZrTe_5$, in which the trigonal prismatic chains of $ZrTe_3$ run along the a axis and are connected with each other by zigzag Te atoms along the c axis, forming a two-dimensional layer of $ZrTe_5$ in the ac planes. These two-dimensional layers of $ZrTe_5$ are stacked together via weak van der Waals interaction to form a 3D $ZrTe_5$ crystal. The interlayer bonding energy is as low as graphite (∼12 meV/Å^2), making it suitable for 2D cleaving [1]. Figure 1(b) shows the image of $ZrTe_5$ single crystals grown by the CVT and flux-growth method. Both crystals are featured in needlelike morphology with the longest direction along the crystallographic a axis. The CVT crystals are relatively larger in comparison with the flux crystals. Figure 1(c) displays the temperature dependence of a-axis resistivity $\rho(T)$ of both single crystals, showing dramatic different behaviors, i.e., the CVT crystal shows a pronounced peak in $\rho(T)$ at $T_p \sim 131$ K, while the $\rho(T)$ of flux-grown crystals remains semiconducting throughout the measured temperature range. In Fig. 1(d), we have plotted the temperature dependence of thermopower $S(T)$ for both crystals. Like the resistivity, the $S(T)$ also shows distinct behaviors for these two crystals. The $S(T)$ of the CVT crystal displays a sign change at T_p from the high-temperature p-type to low-temperature n-type dominated charge carriers, while the $S(T)$ of the flux crystal remains positive in the entire investigated temperature range (2–300 K). It is important to note that the values of thermopower at room temperature for both crystals are similar ∼200 $\frac{\mu V}{K}$, which is relatively high among known thermoelectric materials.

B. Transport properties at high pressures

To investigate the effect of pressure on the transport properties of $ZrTe_5$, we measured $\rho(T)$ and $S(T)$ of both crystals at different pressures up to 20 kbar in the temperature range $2 < T < 300$ K. Figure 2(a) shows the $\rho(T)$ of the CVT-grown crystals under different pressures up to 18.2 kbar. We found that the resistivity exhibits a dramatic enhancement with increasing pressure throughout the entire temperature range, except at low temperatures below 50 K. Notably, the magnitude of ρ at T_p rises significantly, reaching as high as five times its ambient-pressure value at 18.2 kbar. In addition, T_p varies nonmonotonically with pressure, i.e., it first increases with pressure up to 12 kbar and then decreases slightly at 18.2 kbar. Near room temperature, a slight increment of ρ is also observed though it is less pronounced compared to that at T_p. Figure 2(b) shows the $S(T)$ of the CVT-grown crystal at different pressures. At all pressures, $S(T)$ changes sign at T_p from positive to negative upon cooling down from room temperature. In line with the resistivity results in Fig. 2(a), the magnitude of thermopower peaks on both sides of T_p also increases with pressure, especially the one below T_p, which is nearly triply enhanced. In addition, the magnitude of S at room temperature increases continuously with increasing pressure,

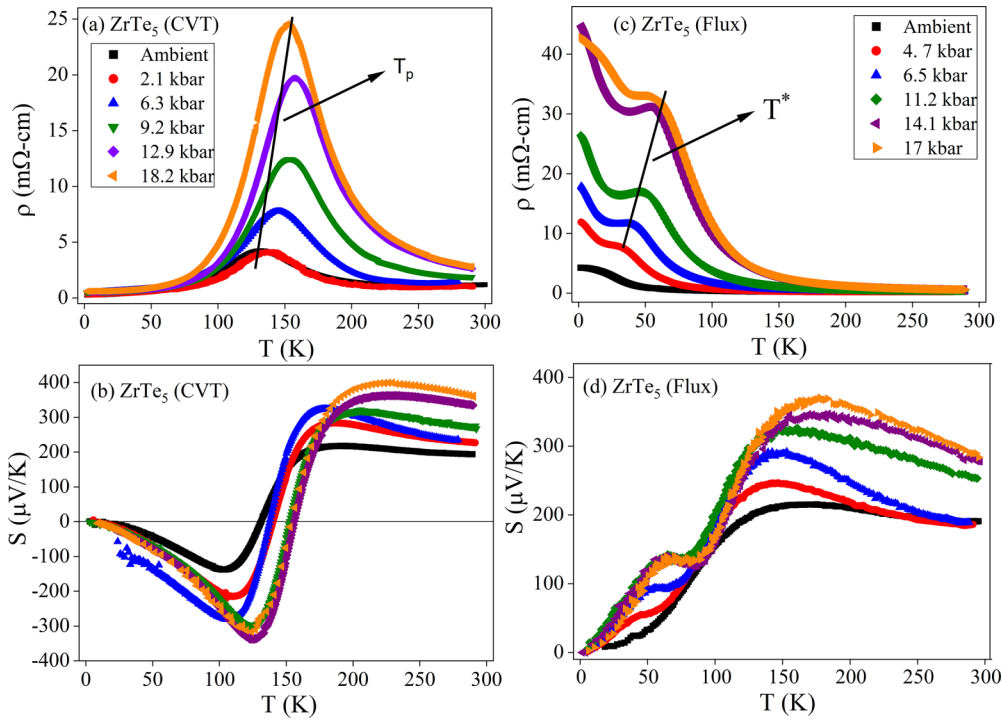

FIG. 2. Temperature dependences of resistivity and thermopower for (a), (b) the CVT and (c), (d) the flux-grown $ZrTe_5$ crystals at different pressures.

revealing an ∼86% enhancement at 18.2 kbar compared to that at ambient pressure.

For comparison, we plotted the $\rho(T)$ and $S(T)$ of the flux-grown $ZrTe_5$ crystals at different pressures in Figs. 2(c) and 2(d), respectively. As seen in Fig. 2(c), $\rho(T)$ is significantly enhanced by pressure, especially at low-temperature regions. In addition, a hump-like feature appears at T^* in $\rho(T)$ at pressures above 4.7 kbar and this feature becomes more evident and moves towards higher temperatures in a fashion similar to the resistivity peak in the CVT crystals. Accordingly, $S(T)$ of the flux-grown sample also exhibits dramatic changes. The $S(T)$ remains positive in the whole investigated temperature and pressure range, indicating the dominant hole carriers. In concomitant with the emergence of resistivity hump, a shoulder-like feature appears near T^* in $S(T)$, moves to higher temperatures and becomes more evident with increasing pressure. S attains a maximum at ∼150 K, and its magnitude increases significantly from 200 to 350 μV/K as pressure increases from ambient to 17 kbar. In addition, S is enhanced by more than 50% in a broad temperature range 150–290 K.

C. Magnetotransport properties at high pressures

Previously, we have studied the longitudinal MR and Hall resistivity (ρ_{xy}) for both CVT and flux-grown crystals at ambient pressure [10]. For the CVT sample at ambient pressure, MR at 1.8 K reaches up to ∼900% at 5 T, decreases to about 100% at 100 K and then increases to ∼400% up to 170 K upon increasing temperature. Also, the MR at $T \leqslant 10$ K exhibits pronounced SdH quantum oscillations. In accordance with $S(T)$, the $\rho_{xy}(H)$ shows negative slope at $T < T_p$ because of the dominance of electron carriers and changes to a positive slope at all $T > T_p$. At T_p, the $\rho_{xy}(H)$ at low field shows a positive slope because of the presence of high-mobility hole carriers and it then changes to a negative slope because of the high-density electron carriers. In contrast to the CVT samples, the MR of the flux-grown samples exhibits a saturation behavior at ambient pressure. The maximum value of MR ∼760% at 5 T was achieved at 100 K. At all temperatures, the $\rho_{xy}(H)$ exhibits a positive slope because of the dominant hole carriers, in line with the $S(T)$ data.

To understand the impact of pressure on the physical properties observed above, we measured MR and ρ_{xy} for both CVT and flux-grown crystals at a few selected temperature and pressures using cubic anvil high-pressure cell. Figures 3(a) and 3(b), and 3(c) and 3(d) show the MR and ρ_{xy} of the CVT crystals at 10 and 20 kbar, respectively. For both samples, the MR is suppressed dramatically as the pressure increases. For the CVT sample at 1.5 K and 5 T, the MR ∼55% at 10 kbar decreases to ∼25% at 20 kbar. The maximum value of MR ∼70% at 5 T takes place at 155 K under 10 kbar, while it decreases to ∼50% at 110 K under 20 kbar. For the flux crystals, in comparison with the MR at 1.8 K and 5 T under ambient pressure, the corresponding MR value has been suppressed to roughly half at 10 kbar and nearly one-fourth at 20 kbar. The maximum value of MR ∼450% at 5 T is found to take place at 100 K under 10 kbar and it decreases to ∼200% at 20 kbar. These observations of pressure-induced suppression of MR are consistent with the previous reports [23,27]. MR at low temperature also exhibits power-law dependence on magnetic field under pressure, MR $\propto H^n$, where n ∼1.5(0.8) for the CVT (flux) crystals. For ρ_{xy}, the magnetic field dependence at high pressure is quite similar to that at ambient pressure, except that the magnitude is diminished gradually with pressure.

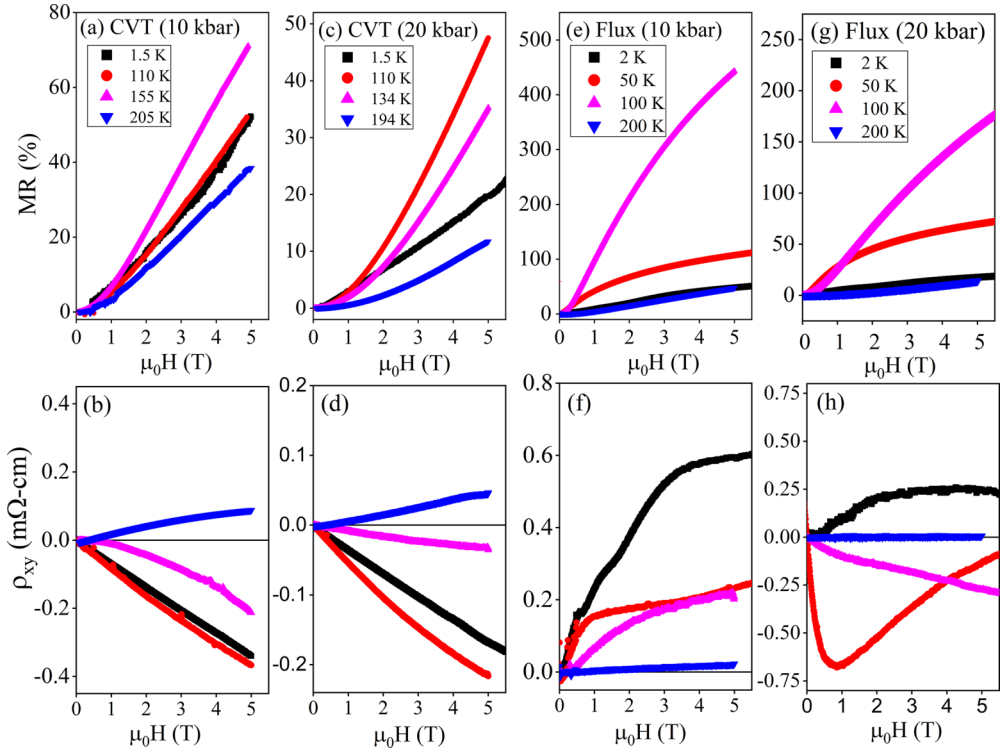

FIG. 3. Field dependence of MR and ρ_{xy} at (a)–(d)10 kbar and (e)–(h) 20 kbar of the CVT and flux-grown $ZrTe_5$ crystals.

To obtain more insights into the evolution of transport behaviors, we employed a two-carrier model to fit the Hall conductivity, $\sigma_{xy} = \frac{\rho_{xy}^2}{\rho_{xx}^2+\rho_{xy}^2}$, as done previously for the data at ambient pressure, viz.,

$$\sigma_{xy}(B) = eB(\pm\frac{n_1\mu_1^2}{(1+\mu_1^2B^2)} \pm \frac{n_2\mu_2^2}{(1+\mu_2^2B^2)}. \quad (1)$$

Here, + (–) gives the hole (electron) contributions, the parameter n and μ give the effective carrier density and mobility for each type of carriers, which refers to the electronic density of states near the Fermi level governing transport phenomenon. Figure 4 illustrates the carrier density and mobility for the CVT and flux-grown crystals at different pressures. For comparison, we have also plotted the ambient-pressure n and μ from our previous study [10]. Figure 4(a) presents the n and μ of the CVT sample at ambient pressure taken from our previous study [10]. The solid symbol stands for electrons and open symbols represent holes. As can be seen, two types of electron carriers, e_1 and e_2, are present at $T < T_p$, while one electron (e_1) and one hole (h_1) carrier with high mobility coexist at T_p. The density of holes increases at $T > T_p$. Upon applying pressure on the CVT crystals, the carrier density was moderately increased, while the mobility was reduced roughly to around one third of the value at ambient pressure. The vertical dashed lines in Figs. 4(a)–4(c) represent the location of T_p for the CVT-grown $ZrTe_5$ single crystals.

For the flux samples, the carrier density at ambient pressure is about two orders lower than that of the CVT samples because of the difference in Te concentrations. As the temperature is raised at ambient pressure, the carrier density increases while the mobility only changes moderately. Upon applying pressure, the carrier density keeps increasing and reaches as high as $\sim 10^{27}\,m^{-3}$, while the mobility decreases to as low as $\sim 0.2\ \frac{m^2}{Vs}$. Additionally, the application of high pressure creates an electron-type carrier in the flux crystals, as seen directly from the $\rho_{xy}(H)$ data at 20 kbar, Fig. 3(h). These data reveal that the application of high pressure produces a notable change in the electronic band structure across the investigated pressure range. The vertical dashed lines in Figs. 4(e) and 4(f) depict the T^* for the flux-grown crystals determined above.

D. Shubnikov-de Haas (SdH) quantum oscillation under pressure

One key difference between the CVT and flux-grown crystals is manifested in the SdH oscillations. For the CVT crystals, quantum oscillations are clearly visible in the field dependence of MR at ambient and high pressures. In contrast, quantum oscillations are absent in the flux-grown crystals. Therefore, we investigated the SdH oscillations in the CVT-grown crystals at selected pressures. Figures 5(a)–5(c) present the background-subtracted $\Delta\rho_{xx}$ extracted from the longitudinal MR as a function of $1/B$ at ambient pressure, 20 and 30 kbar, respectively. The corresponding fast Fourier transformations (FFT) at each pressure are shown in the inset. As the pressure increases, the oscillations start to appear at higher magnetic field and the corresponding FFT reveals an increase in the frequency suggesting the increase in the FS area. The analysis of the temperature-dependent FFT amplitude revealed an increase in the effective mass. The FS cross sectional area calculated using the Onsager relation, $S_F = \frac{2\pi e}{\hbar}\alpha$ (where α is the FFT frequency) increases by

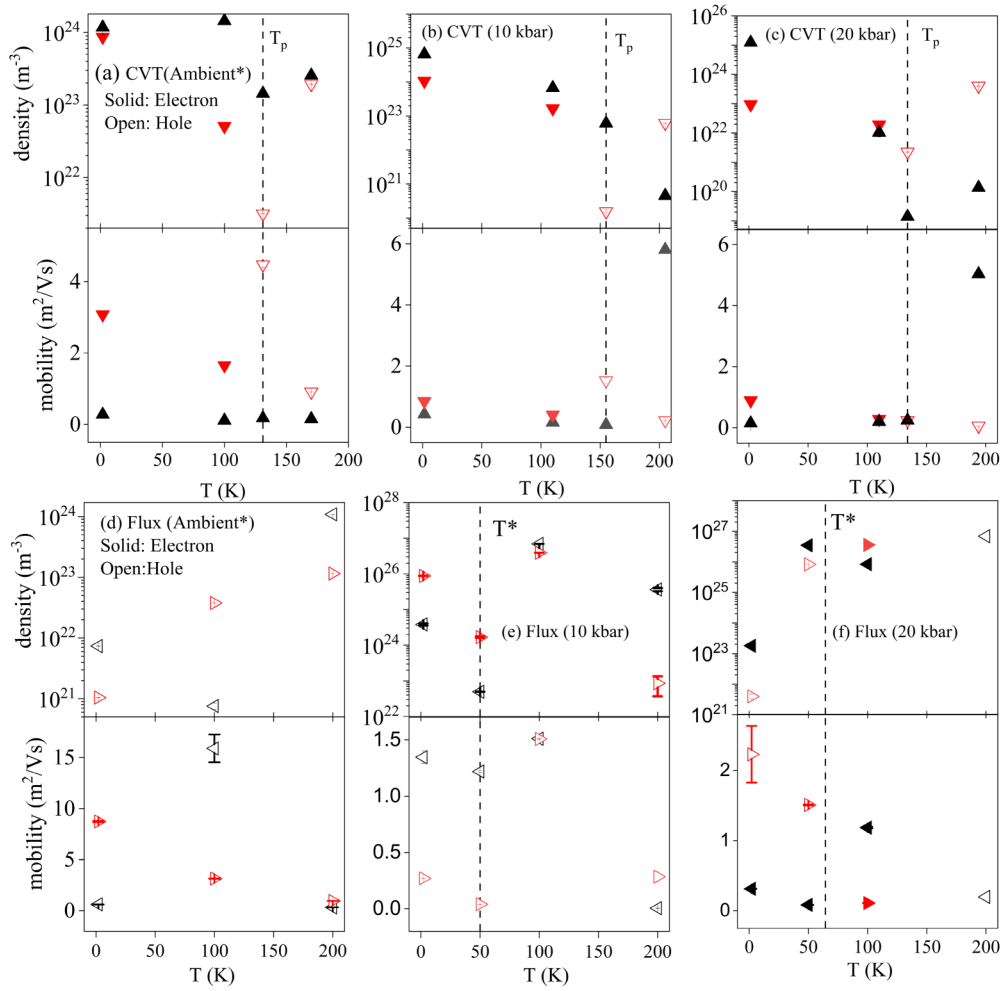

FIG. 4. Carrier density and mobility of (a)–(c) the CVT and (d)–(f) the flux-grown crystals at ambient, 10 and 20 kbar, respectively. For comparison, we have taken the ambient-pressure data from our previous study [10]. Vertical dashed lines depict the location of T_p and T^* for the CVT and flux-grown crystals, respectively.

about six times from 3.99×10^{-4} Å^{-2} at ambient pressure to 2.69×10^{-3} Å^{-2} at 30 kbar. Similarly, the m^* also increases by four times.

To estimate different parameters related to FS, we analysed the SdH oscillations according to the Lifshitz-Kosevich (LK) theory [8,38,39], which describes the reduction of SdH oscillation amplitude with increasing temperature by the formula, viz.,

$$\Delta\rho_{xx} \propto R_T R_D R_S \cos\left(2\pi\left(\frac{\alpha}{B}+\beta\right)\right), \tag{2}$$

where R_T, R_D, and R_S are three reduction factors responsible for smearing out the oscillations caused by temperature, scattering, and spin-induced splitting, respectively. Temperature dependence of the oscillation is described by

$$R_T = \frac{\lambda(T)}{\sinh\lambda(T)}, \tag{3}$$

where $\lambda(T) = \frac{2\pi^2 m_* k_B T}{\hbar e B}$ and m^* is the cyclotron mass. Figure 5(d) shows the fitting of Eq. (2) to $\Delta\rho_{xx}(T)/\Delta\rho_{xx}$ vs T at ambient, 20, and 30 kbar. Quantum lifetime of carriers contributing to SdH oscillation can be determined experimentally using the Dingle plot [40,41]. According to the Lifshitz-Kosevich theory, the amplitude of SdH oscillation decreases because of scattering as given by

$$R_D = \frac{\Delta\rho_{xx}}{\rho_0} = \frac{4\lambda e^{-\lambda_D}}{\sinh(\lambda)}, \tag{4}$$

where ρ_0 is the resistivity of $ZrTe_5$ in zero magnetic field, and $\lambda_D = \frac{2\pi^2 m_* K_B T_D}{\hbar e B}$ and $\lambda = \frac{2\pi^2 K_B T m_*}{\hbar e B}$. Here, $T_D = \frac{\hbar}{2\pi K_B \tau}$ is called Dingle temperature and τ is the total scattering time of carriers. Figure 5(e) shows a graph of $\ln[\frac{\Delta\rho_{xx}\sinh(\lambda)}{4\rho_0\lambda}]$ vs $1/B$ at 20 and 30 kbar. The inset shows the same plot for the ambient pressure. The estimated cyclotron mass (m^*) and quantum mobility (μ) are summarized in Fig. 5(f). It is clear that m^* increases almost four times as pressure increases to 30 kbar. At the same time, the quantum mobility is reduced to almost half. The details of Berry phase calculations at different pressure have been discussed in Appendix A 2. The analysis of SdH oscillations for the CVT samples are consistent with the results obtained from the two-band model fitting to the magnetotransport data as discussed in the previous section.

E. Computation results: Band structure and density of states

To obtain further insight into the underlying phenomena, we performed density functional theory band-structure

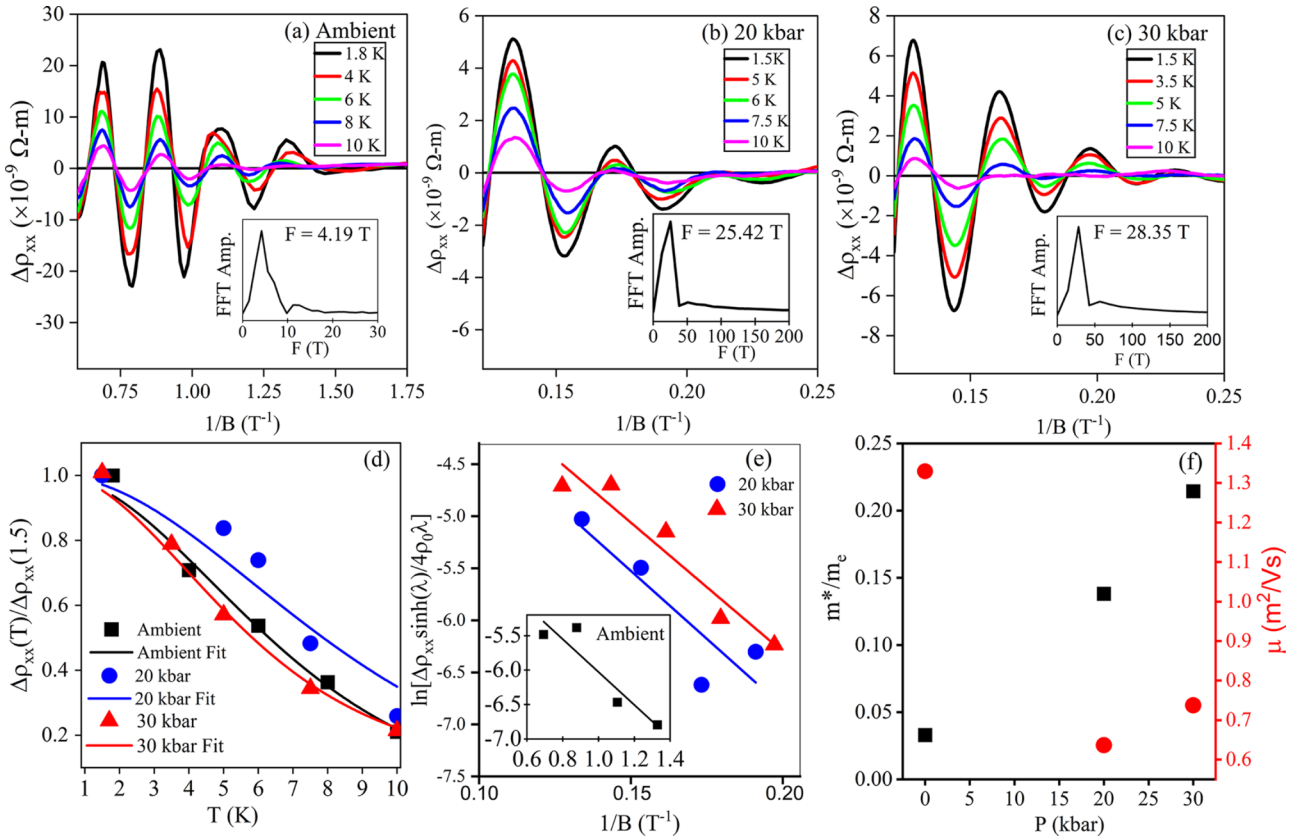

FIG. 5. (a)–(c) The SdH oscillations of the CVT samples below 10 K at ambient, 20, and 30 kbar respectively. The inset shows the amplitude vs frequency of fast Fourier transformations (FFT) of corresponding oscillations. (d) Temperature-dependent damping of normalised amplitude of oscillations at ambient, 20, and 30 kbar. The solid curves represent the fitting of $\Delta\rho_{xx}(T)/\Delta\rho_{xx}(T_{min})$ vs T according to the Lifshitz-Kosevich theory as described in Eq. (3). (e) The Dingle plot at 20 and 30 kbar. The solid straight line shows the fitting according to Eq. (4). Inset in (e) shows the corresponding data for ambient pressure. (f) Calculated cyclotron mass (m^*) and quantum mobility of carries at different pressures.

calculations. Figure 6(a) displays the Brillouin zone of $ZrTe_5$ centred at Γ point, which highlights the high-symmetry points used for band-structure calculations. Figure 6(b) illustrates the calculated total density of states (DOS) near the Fermi level at three pressures, i.e., ambient, 10, and 20 kbar. The DOS profile provides insight into the pressure-induced changes in electronic structure near the Fermi level. In Figs. 6(c)–6(e), we present the calculated electronic band structure of $ZrTe_5$ under ambient, 10, and 20 kbar pressure, respectively. At ambient pressure, the conduction band minimum (CBM) and the valance band maximum (VBM) touch exactly at the Γ point, revealing the formation of gapless Dirac-like band dispersion near the Fermi level, consistent with previous experimental observations [5,13,15,16,42,43]. This feature is also visible by the presence of a finite DOS near the Fermi level at ambient pressure. As pressure is increased to 10 kbar, the system seems to undergo a phase transition with a noticeable increase in band gap of ∼70 meV. The direct band gap at Γ point continues to widen further to 90 meV at 20 kbar in agreement with the previous report [1,25]. Also, Figs. 6(c)–6(e) show a clear band reorganization with pressure near the Γ point, characterized by band warping along the Γ-Y and Γ-Z high-symmetry directions. A similar effect is also visible along the Γ-X direction. Although, the pressure-induced band-structure evolution is modest, it is consistent with the increase in DOS near the Fermi level. This feature aligns with the pressure-induced enhancement in carrier density; however, the magnitude of the change seems to be insufficient to account for the drastic increase in the effective carrier density as derived from the Hall conductivity measurements.

IV. DISCUSSION

The difference in the transport properties between the CVT and flux-grown $ZrTe_5$ crystals at ambient pressure arises from the different Te content. In general, the CVT-grown crystals are Te deficient, which acts as an *n*-type dopant leading to higher carrier density [Figs. 4(a) and 4(d)]. Furthermore, in CVT-grown crystals, the dominant carrier changes from hole to electron across T_p, while near T_p both types of carriers participate simultaneously in transport, enabling bipolar conduction, whereas the flux-grown crystals are close to stoichiometry, hence displaying intrinsic unipolar *p*-type conduction [10]. Despite this difference, the application of external pressure results in a similar overall enhancement of ρ and S for both types of crystals. Figure 7 summarises the pressure dependence of ρ at selected temperature (2 K, T_p/T^* and 290 K) for CVT [Fig. 7(a)] and flux-grown [Fig. 7(b)] crystals. In Fig. 7(c), we show the pressure dependence of S at 290 K for both crystals, while Fig 7(d) shows the variation of

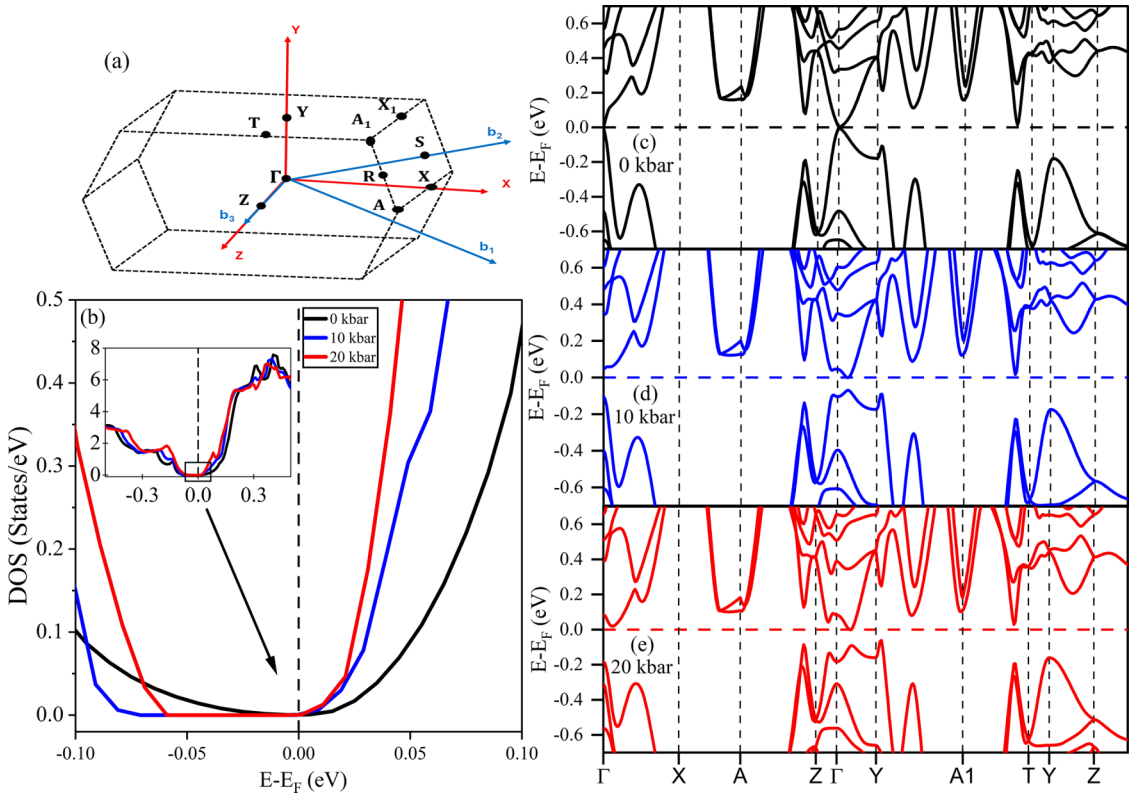

FIG. 6. (a) The Brillouin zone of $ZrTe_5$ along with high-symmetry points used in calculations of bands. (b) Total density of states per eV of $ZrTe_5$ near the Fermi level at different pressures, ambient, 10, and 20 kbar. (c)–(e) The calculated electronic band structures at ambient, 10, and 20 kbar, respectively.

T_p and T^*. The ρ enhancement is more pronounced at T_p for the CVT crystal and at low temperatures for the flux-grown crystals as shown in Figs. 7(a) and 7(b). For the flux-grown crystals, the ρ remains semiconducting up to 18 kbar, but a broad hump-like feature at T^* appears in $\rho(T)$ above a moderate pressure (4.7 kbar) [Fig. 2(c)]. Like T_p, T^* gradually shifts towards higher temperatures with increasing pressure [Fig. 7(d)]. Variation of S with pressure near room temperature

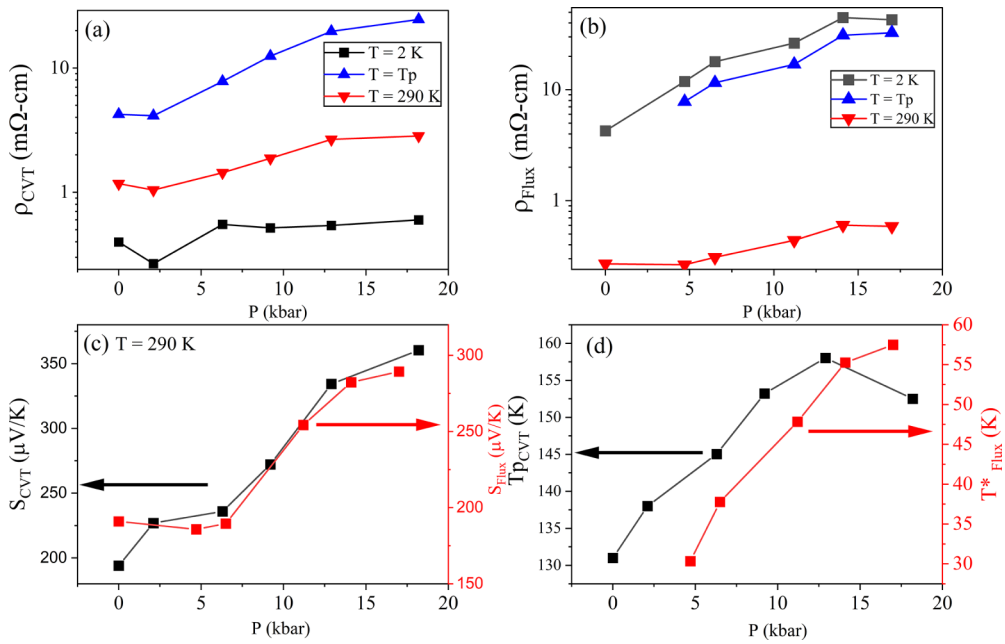

FIG. 7. Variation of resistivity with pressure at some selected temperatures 2 K, T_p, and 290 K for (a) CVT and (b) flux-grown crystals. Pressure dependences of thermopower at 290 K and T_p for (c) the CVT and (d) flux-grown crystals.

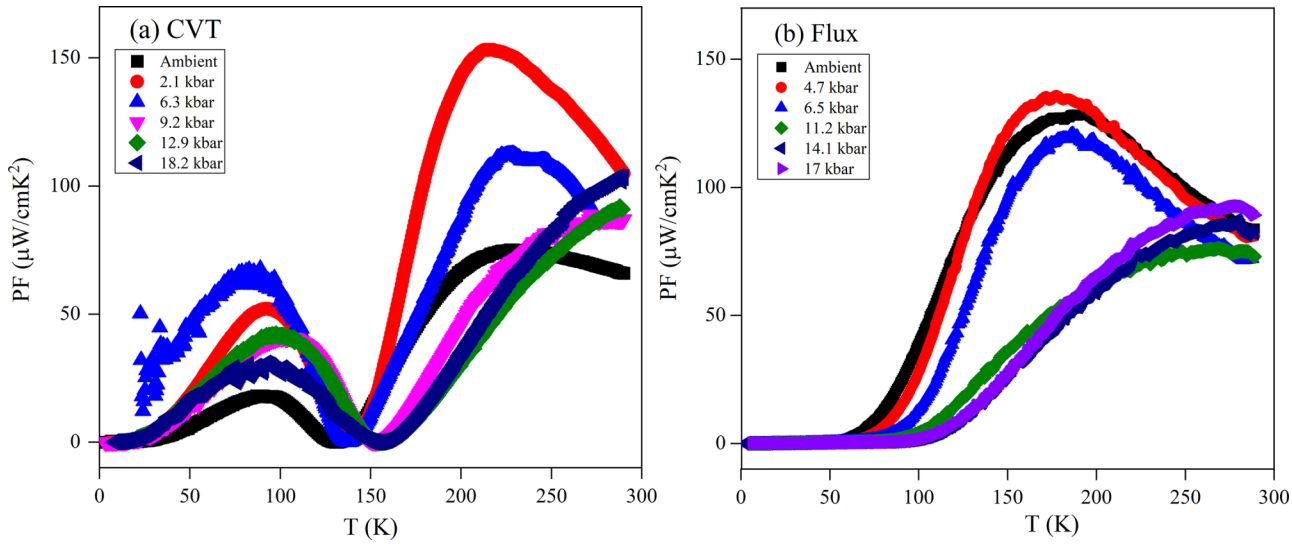

FIG. 8. Thermoelectric power factor as function of temperature of the (a) CVT and (b) flux-grown crystals at different pressures.

is almost similar in both types of crystals [Fig. 7(c)]. However, unlike the CVT-grown crystals, the S does not change sign at T^* in the flux-grown samples, but instead displays a shoulder. The sign change of S and Hall coefficient at T_p occurs because of the compensation of the electron and hole carriers. The absence of sign changes in the flux-grown crystals suggests that the carriers are not exactly compensated, but electron-like carriers also contribute to the charge transport in addition to the hole-type. This is also evident from the sign change of ρ_{xy} around 50–100 K at 20 kbar as in Fig. 3(h). These observations indicate that with the application of pressure the charge conduction changes from unipolar to bipolar nature in flux-grown crystals. This is further bolstered by the appearance of a peak-like feature in $R(T)$ at 40 kbar in the flux-grown crystals (Fig. 9). In general, T_p in the $ZrTe_5$ single crystals is associated with the Fermi level, which depends on the carrier concentration [26]. Analyses of the magnetotransport properties reveal qualitatively similar impact of pressure on both crystals, i.e., the increase of carrier concentration, resulting the enhancement of T_p and T^* with pressure. Here, the sharp enhancement in carrier density derived from fitting of σ_{xy} (Fig. 4) is not mirrored by band-structure evolution in DFT results (Fig. 6). This can be understood in terms of both the sensitivity of magnetotransport measurements and the limitations in the DFT approach. In dilute semimetals like $ZrTe_5$, the transport properties are highly sensitive to small shifts in band energies, even a slight pressure driven tuning of lattice parameters may result in a reorganization of band edges across the Fermi level, which could possibly be underestimated in DFT causing an increase in the number of thermally activated carriers. On the other hand, the carrier density extracted from σ_{xy} using a two-carrier model reflects an effective density that is dominated by carriers from higher mobility bands. Application of pressure can strongly influence mobility by changing scattering parameters or altering the band curvature, and thus the carrier density can be amplified in transport measurements. In fact, this phenomenon is not unique in ZrTe5, but there are several examples of low-dimensional semimetals (e.g., black phosphorus [44], $TaTe_4$ [45], $HfTe_5$ [46]), where the application of a moderate pressure enhances the effective carrier density prior to any crystallographic changes. Additionally, the DFT calculations capture an idealized bulk crystal of $ZrTe_5$, while its real samples are known to host additional conducting channels from surface states [1]. Pressure may enhance these surface contributions, providing parallel conduction paths that further increase the Hall response beyond the bulk picture captured in our calculations.

In Fig. 8, we have shown the thermoelectric power factor ($PF \equiv S^2/\rho$) of the CVT and flux-grown $ZrTe_5$ crystals at different pressures. The PF of the CVT crystals displays a nonmonotonic variation as a function of pressure in the entire temperature region. In addition, it is approximately twofold higher in the semiconducting region ($T > T_p$) than in the metallic region ($T < T_p$) at all pressures. In contrast, the PF of flux-grown crystal exhibits an almost decreasing trend with pressure. At room temperature, the decrease in PF is moderate, while below the room temperature, the PF reduction is dramatic, decreasing to almost half near 150 K. Furthermore, on applying a moderate pressure, the room-temperature PF of the CVT-grown $ZrTe_5$ crystals exhibit a dramatic enhancement of ∼56.5% at 18.2 kbar. On the other hand, the flux-grown crystals show only a weak increase of 6.2% at 17 kbar pressure. Apart from the room temperature, it is also worthwhile to discuss the behavior of PF below and above T_p (or T^*). S shows dramatic enhancement around T_p or T^*; however, because of the sign change of S across T_p in the CVT crystals, the PF diminishes at T_p. But above and below T_p, PF is almost enhanced by a factor of 2. On the other hand, the PF of the flux-grown crystals decreases to one-third of that at ambient pressure.

Furthermore, it is worthwhile to discuss the thermoelectric figure of merit $ZT = S^2T/\kappa\,\rho$ for this $ZrTe_5$ system, which is important for the overall thermoelectric efficiency. In general, thermal conductivity (κ), of a material consists of two parts: electronic term κ_e, and phonon contribution κ_{ph}. We can use the Widemann-Franz law to reasonably estimate the effect of pressure on electronic part of thermal conductivity, i.e., $\kappa_e = LT/\rho$, where L is Lorentz number. Since in our case, the

overall temperature dependence of resistivity (ρ) was found to increase with pressure, it directly implies that the κ_e term is expected to decrease. Near room temperature (290 K), κ_e reduces around 55% up to 20 kbar pressure for both types of crystals. Unlike the κ_e, lattice thermal conductivity (κ_{ph}) is more sensitive to the phonon dynamics. As pressure increases, the atomic orbital overlap intensifies, leading to the phonon hardening effect, which typically increases the phonon velocity and reduces phonon scattering and therefore increases κ_{ph}. The overall trend of thermal conductivity (κ) depends on the relative change of κ_e vs κ_{ph}. Thus, the net impact of pressure on ZT will depend on the relative magnitude of these opposing quantities.

Engineering of carrier density and mobility can play a crucial role in the optimization of the thermoelectric performance of a material [47–49]. In general, the relationship for $\rho(T)$ and $S(T)$ in the presence of electrons and holes can be given by [50] $\rho(T) = \frac{1}{e(n_e\mu_e + n_h\mu_h)}$, $S = \frac{k_B}{e}.\frac{n_hA^h - n_eA^n}{n_h + n_e}$, where $n_{e(h)}$, $\mu_{e(h)}$ are the density and mobility of elections (holes), k_B is the Boltzmann constant, e is the electronic charge, $A^{h(e)}$ represents average contribution in thermopower from holes (electrons). The pressure induced interplay between density and mobility causes the enhancement in resistivity and thermopower. On the other hand, the observed decrease in mobility with pressure suggests that carriers are becoming heavier, indicating the enhancement of effective mass under pressure. This increase in effective mass could be the reason for the significant increase in thermopower. In fact, this expectation is consistent with the quantum oscillation data of $ZrTe_5$ under pressure as shown in [27] and the theoretical calculations in Refs. [21,27]. Furthermore, given the Dirac semimetallic nature of $ZrTe_5$ at ambient pressure, it is essential to discuss thermoelectric properties through the framework of Dirac band dispersion. Dirac materials exhibit linear band dispersion near the Fermi level, which typically enhances carrier mobility and favors a large Seebeck coefficient becauseof energy-dependent density of states and carrier velocity [47]. In $ZrTe_5$, this Dirac-like behavior contributes to the high thermopower [S ∼200 μV/K at 300 K, Fig. 1(d)] observed in both CVT and flux-grown crystals. Under pressure, however, our band-structure calculations (Fig. 6) reveal a transition from Dirac semimetal to a gapped phase, evidenced by the opening of a direct bandgap at Γ. This is corroborated by Berry phase analysis (Appendix A 2), which shows a shift from nontrivial to trivial topology. The suppression of Dirac dispersion under pressure reduces carrier mobility (Fig. 4) but simultaneously enhances the effective mass Fig. 5(f) and density of states near the Fermi level Fig. 6(b), leading to the anomalous concurrent increase in S and ρ. Such behavior is rare in conventional thermoelectrics highlights the role of Dirac physics in governing the thermoelectric response. The pressure-induced topological transition thus provides a unified framework for understanding the optimization of PF in ZrTe5, particularly in CVT-grown crystals where PF doubles at 18.2 kbar. In addition, the resistivity increases and low-temperature upturn in the flux-grown crystals with the application of pressure should be attributed to the band-gap opening under compression, as indicated by our DFT calculation for stoichiometric $ZrTe_5$ crystal, in good agreement with previous studies [48,21]. These results demonstrate the promise of $ZrTe_5$ as a candidate for thermoelectric energy conversion. Moreover, this will pave the way to explore the thermoelectric performance of $ZrTe_5$ in the two-dimensional limit.

V. CONCLUSIONS

The objective of this study was to investigate the effect of high pressure on the transport properties of CVT and flux-grown $ZrTe_5$ single crystals. We find that the application of pressure has significantly changed transport properties of $ZrTe_5$ depending on the growth method. While the CVT-grown $ZrTe_5$ displays bipolar transport near T_p, the flux crystals also show bipolar transport character under pressures. The Te vacancies in the CVT crystals can be considered as a form of chemical pressure; however, the emergence of bipolar transport characteristic in flux-grown crystals marked by the emergence of resistivity peak (T^*) resembles that of CVT crystals, which highlights the equivalence of physical and chemical pressure effects. Transport measurement along with complementary first-principles band-structure calculations demonstrated the pressure-induced opening of a direct band gap at Γ point with a decreased DOS near the Fermi level. The analysis of the magnetotransport results at various pressures revealed an increase of carrier concentration and a decrease in carrier mobility coupled with an increase in effective mass. Additionally, the application of pressure has been found to enhance the *PF* of CVT-grown $ZrTe_5$ single crystals by more than 50%, whereas the *PF* enhancement is moderate, ∼6% for the flux-grown crystal at room temperature. The above findings offer an understanding how different growth methodologies and application of pressure may affect the electronic properties of $ZrTe_5$ and therefore provide a framework for designing materials with tailored thermoelectric performance.

ACKNOWLEDGMENTS

S.M. acknowledges support from Science and Engineering Research Board (SERB), India, for the Junior Research Fellowship (File No. SRG/2019/001187). V.K.G. acknowledges SERB India for the award of SERB International Research Experience (SIRE) fellowship (File No.- SIR/2022/000804). P.S. acknowledges SERB India for award of Start-Up Research Grant (SRG/2019/001187), University Grant Commission (UGC) for Basic Scientific Research (BSR) fund (UGC File No.- 30–505/2020(BSR)), UGC-DAE Centre for providing funds (CRS/2021–22/01/415) and SERB India for SERB-SIRE fellowship (File No.- SIR/2022/000752). J.G.C. is supported by National Key Research and Development Program of China (No. 2023YFA1406100, 2021YFA1400200), National Natural Science Foundation of China (No. 12025408, U23A6003), and CAS PIFI program (2024PG0003).

DATA AVAILABILITY

The data that support the findings of this article are not publicly available. The data are available from the authors upon reasonable request.

APPENDIX

1. $ZrTe_5$ (Flux) data at 40 kbar pressure

Figure 9 presents the longitudinal resistance $R(T)$ and Hall resistance R_{xy} ($T = 2$ K) of the flux-grown crystals at 40 kbar in a cubic anvil cell. It exhibits similar behaviors as that of the CVT-grown crystals.

2. Berry Phase calculation

For estimating the change in Berry phase with pressure, we have applied the Lifshitz-Onsager quantization rule [51–53] to analyze the quantum oscillations. According to this rule, each peak and valley of the quantum oscillation can be indexed by Landau level (n) as a function of $1/B$. Figure 10 depicts the plot of Landau level peak index (n) vs the inverse of the magnetic field ($1/B$) at 0, 20 and 30 kbar pressure. For the calculation of peak index (n), we multiplied the values of $1/B$ at each peak and valley of oscillation by the FFT frequency. Linear fitting of the Fan diagram gives

$$\frac{\alpha}{B} = n + \beta,$$

where α is the slope of the Fan diagram, which provides details about Fermi surface. The intercept β gives information about Berry phase of the system. The intercept β can be expressed in terms of the Berry phase as

$$\beta = \frac{1}{2} + \delta - \frac{\varnothing_B}{2\pi},$$

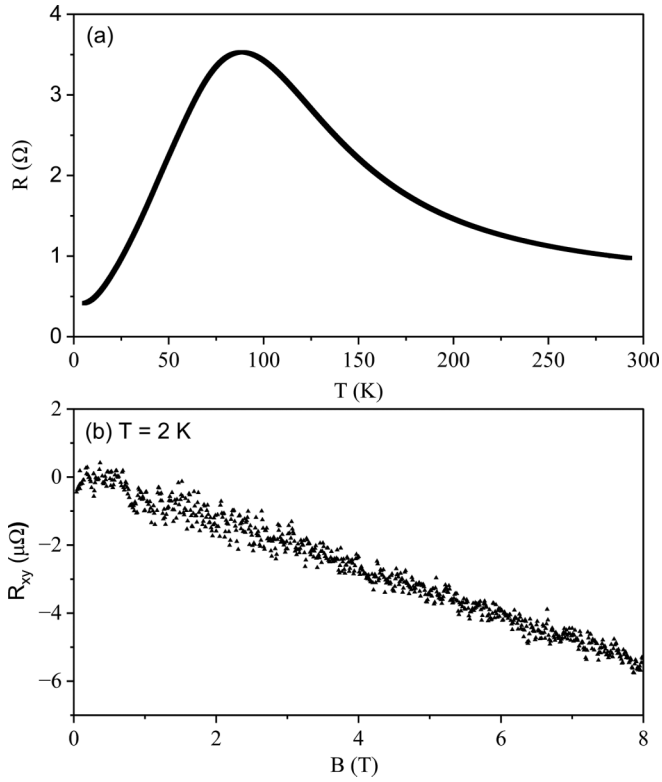

FIG. 9. The longitudinal and Hall resistance of the flux-grown $ZrTe_5$ crystals at 40 kbar.

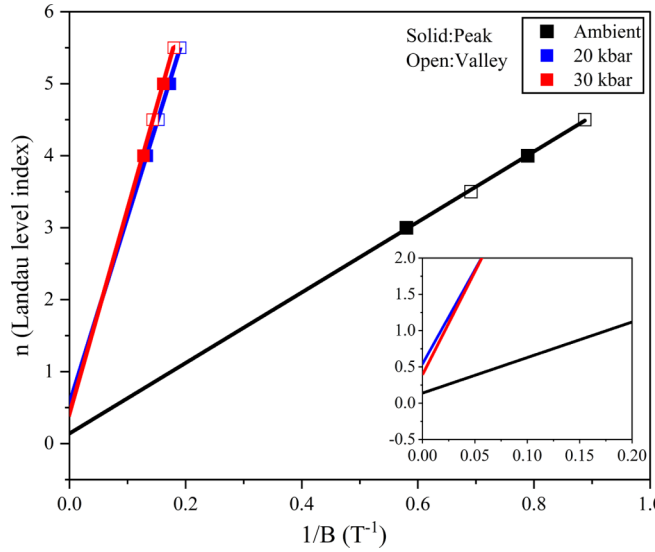

FIG. 10. Landau level index (n) vs $1/B$ at different pressures. Inset shows closer view of intercepts at $1/B = 0$.

where $\varnothing_B$ is the Berry phase shift. Here, δ is an additional phase arising as a result of the degree of dimensionality of the materials. For 2D materials, $\delta = 0$, whereas for 3D materials its value lies between $+\frac{1}{8}$ and $-\frac{1}{8}$. If the value of intercept $|\beta|$ is $0 \pm \frac{1}{8}$, in this case $\varnothing_B = \pi$ is a called trivial Berry phase. When its value is $\frac{1}{2} \pm \frac{1}{8}$, this situation is called a nontrivial Berry phase ($\varnothing_B = 0$) [54,55]. In the present case, from the linear fit of the Landau level fan diagram, the value of $\beta \sim 0$ at ambient pressure, therefore, $\varnothing_B = \pi$, which gives a nontrivial Berry phase. The application of pressure gives $\beta \sim 0.5$, which gives $\varnothing_B = 0$ and therefore a trivial Berry phase under pressure. Therefore, we see a pressure-induced Berry phase shift from nontrivial to trivial.

3. Band structure and Density of States with Experimental lattice constants

We have also calculated the band structure and density of states (DOS) using experimental lattice constant instead of

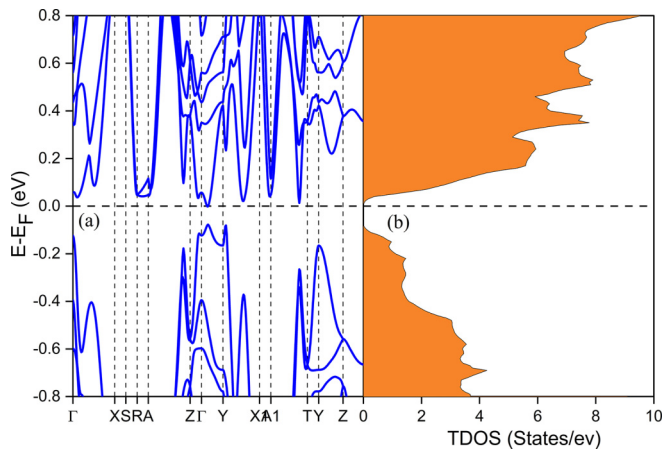

FIG. 11. Band structure and density of states with experimental lattice constant at ambient pressure.

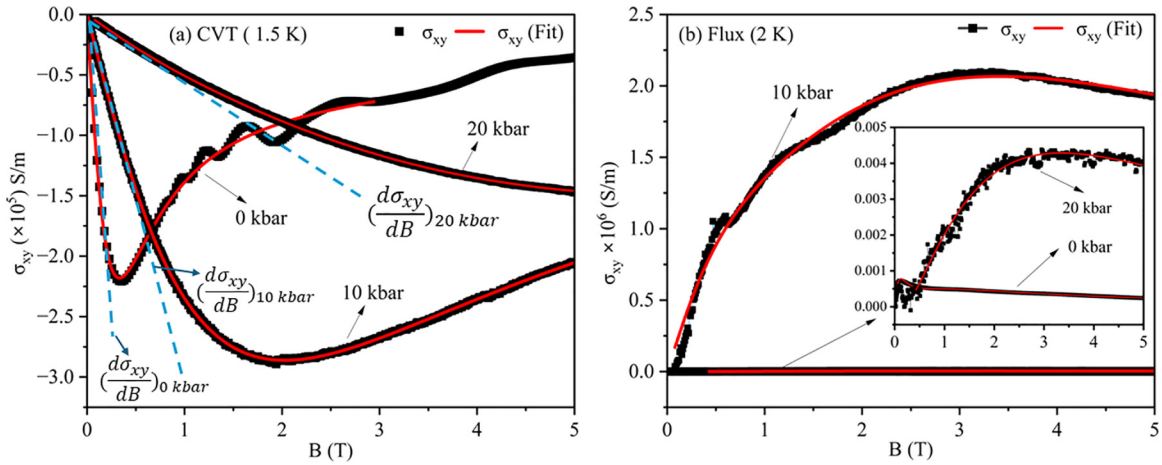

FIG. 12. Hall conductivity (σ_{xy}) as function of magnetic field along with its fitting with two-carrier model. Panels (a) and (b) correspond to CVT and flux-grown crystals, respectively. In panel (a) tangent of σ_{xy} is shown as a dotted line.

optimized one reported in Ref. [10]. As shown in Fig. 11, the band gap at gamma point is nearly 178 meV.

4. Two band model fitting results

We have applied two-band model to extract the carrier density (n_1, n_2) and mobility (μ_1, μ) from the Hall conductivity using the formula

$$\sigma_{xy}(B) = eB(\pm\frac{n_1\mu_1^2}{(1+\mu_1^2B^2)} \pm \frac{n_2\mu_2^2}{(1+\mu_2^2B^2)}.$$

Here, $+(-)n$ stands for hole(electron) density, μ mobility of carriers. The experimental and fitted curves of σ_{xy} at low temperature for CVT and flux-grown crystals at 10 and 20 kbar pressure are shown in Fig. 12.

To cross verify the results shown in Fig. 12, we also analyzed dσ_{xy}/dB, the slope of the $\sigma_{xy}(B)$ curve in low-field region. It is very clear from the figure that with varying pressure slope of $\sigma_{xy}(B)$ curve undergoes dramatic change with increasing pressure, implying a change in carrier concentration, consistent with the above two-band model.

[1] H. Weng, X. Dai, and Z. Fang, Transition-metal pentatelluride $ZrTe_5$ and $HfTe_5$: A paradigm for large-gap quantum spin Hall insulators, Phys. Rev. X **4**, 011002 (2014).

[2] S. Okada, T. Sambongi, and M. Ido, Giant resistivity anomaly in $ZrTe_5$, J. Phys. Soc. Jpn. **49**, 839 (1980).

[3] R. T. Littleton, T. M. Tritt, J. W. Kolis, and D. R. Ketchum, Transition-metal pentatellurides as potential low-temperature thermoelectric refrigeration materials, Phys. Rev. B **60**, 13453 (1999).

[4] M. Rubinstein, $HfTe_5$ and $ZrTe_5$: Possible polaronic conductors, Phys. Rev. B **60**, 1627 (1999).

[5] Y. Wang, H. F. Legg, T. Bömerrich, J. Park, S. Biesenkamp, A. A. Taskin, M. Braden, A. Rosch, and Y. Ando, Gigantic Magnetochiral Anisotropy in the Topological Semimetal $ZrTe_5$, Phys. Rev. Lett. **128**, 176602 (2022).

[6] L. Moreschini, J. C. Johannsen, H. Berger, J. Denlinger, C. Jozwiack, E. Rotenberg, K. S. Kim, A. Bostwick, and M. Grioni, Nature and topology of the low-energy states in $ZrTe_5$, Phys. Rev. B **94**, 081101(R) (2016).

[7] G. N. Kamm, D. J. Gillespie, A. C. Ehrlich, T. J. Wieting, and F. Levy, Fermi surface, effective masses, and Dingle temperatures of $ZrTe_5$ as derived from the Shubnikovde Haas effect, Phys. Rev. B **31**, 7617 (1985).

[8] H. Chi, C. Zhang, G. Gu, D. E. Kharzeev, X. Dai, and Q. Li, Lifshitz transition mediated electronic transport anomaly in bulk $ZrTe_5$, New J. Phys. **19**, 015005 (2017).

[9] Y. Zhang, C. Wang, L. Yu, G. Liu, A. Liang, J. Huang, S. Nie, X. Sun, Y. Zhang, B. Shen *et al.*, Electronic evidence of temperature-induced Lifshitz transition and topological nature in $ZrTe_5$, Nat. Commun. **8**, 15512 (2017).

[10] P. Shahi, D. J. Singh, J. P. Sun, L. X. Zhao, G. F. Chen, Y. Y. Lv, J. Li, J. Q. Yan, D. G. Mandrus, and J. G. Cheng, Bipolar conduction as the possible origin of the electronic transition in pentatellurides: Metallic vs semiconducting behavior, Phys. Rev. X **8**, 021055 (2018).

[11] W. Song, X. Yuan, J. Shen, Y. Xu, F. Wang, X. Zhu, and Y. Zhang, Temperature dependence of band shifts induced by impurity ionization in $ZrTe_5$, Phys. Rev. B **106**, 115124 (2022).

[12] G. Manzoni, A. Sterzi, A. Crepaldi, M. Diego, F. Cilento, M. Zacchigna, Ph. Bugnon, H. Berger, A. Magrez, M. Grioni *et al.*, Ultrafast optical control of the electronic properties of $ZrTe_5$, ultrafast optical control of the electronic properties of $ZrTe_5$, Phys. Rev. Lett. **115**, 207402 (2015).

[13] G. Zheng, J. Lu, X. Zhu, W. Ning, Y. Han, H. Zhang, J. Zhang, C. Xi, J. Yang, H. Du, K. Yang, Y. Zhang, and M. Tian, Transport evidence for the three-dimensional Dirac semimetal phase in $ZrTe_5$, Phys. Rev. B **93**, 115414 (2016).

[14] G. Manzoni, L. Gragnaniello, G. Autès, T. Kuhn, A. Sterzi, F. Cilento, M. Zacchigna, V. Enenkel, I. Vobornik, L. Barba *et al.*, Evidence for a strong topological insulator phase in $ZrTe_5$, Phys. Rev. Lett. **117**, 237601 (2016).

[15] E. Martino, I. Crassee, G. Eguchi, D. Santos-Cottin, R. D. Zhong, G. D. Gu, H. Berger, Z. Rukelj, M. Orlita, C. C. Homes, and A. Akrap, Two-dimensional conical dispersion in $ZrTe_5$ evidenced by optical spectroscopy, Phys. Rev. Lett. **122**, 217402 (2019).

[16] R. Y. Chen, S. J. Zhang, J. A. Schneeloch, C. Zhang, Q. Li, G. D. Gu, and N. L. Wang, Optical spectroscopy study of the three-dimensional Dirac semimetal $ZrTe_5$, Phys. Rev. B **92**, 075107 (2015).

[17] J. Mutch, W. C. Chen, P. Went, T. Qian, I. Z. Wilson, A. Andreev, C. C. Chen, and J. H. Chu, Evidence for a strain-tuned topological phase transition in $ZrTe_5$, Sci. Adv. **5**, eaav9771 (2019).

[18] Q. Li, D. E. Kharzeev, C. Zhang, Y. Huang, I. Pletikosić, A. V. Fedorov, R. D. Zhong, J. A. Schneeloch, G. D. Gu, and T. Valla, Chiral magnetic effect in $ZrTe_5$, Nat. Phys. **12**, 550 (2016).

[19] T. Liang, J. Lin, Q. Gibson, S. Kushwaha, M. Liu, W. Wang, H. Xiong, J. A. Sobota, M. Hashimoto, P. S. Kirchmann *et al.*, Anomalous Hall effect in $ZrTe_5$, Nat. Phys. **14**, 451 (2018).

[20] Z. Kovács-Krausz, D. Nagy, A. Márffy, B. Karpiak, Z. Tajkov, L. Oroszlány, J. Koltai, P. Nemes-Incze, S. P. Dash, P. Makk, S. Csonka, and E. Tóvári, Signature of pressure-induced topological phase transition in $ZrTe_5$, npj Quantum Mater. **9**, 76 (2024).

[21] J. Gao, M. Zhong, Q. J. Liu, B. Tang, F. S. Liu, and X. J. Ma, Effects of pressure on structural, electronic, optical, and mechanical properties of $ZrTe_5$: A density functional theory study, Phys. B: Condens. Matter **620**, 413286 (2021).

[22] M. M. Piva, R. Wawrzyńczak, N. Kumar, L. O. Kutelak, G. A. Lombardi, R. D. Dos Reis, C. Felser, and M. Nicklas, Importance of the semimetallic state for the quantum Hall effect in $HfTe_5$, Phys. Rev. Mater. **8**, L041202 (2024).

[23] Y. Zhou, J. Wu, W. Ning, N. Li, Y. Du, X. Chen, R. Zhang, and Z. Chi, Pressure-induced superconductivity in a three-dimensional topological material $ZrTe_5$, Proc. Natl. Acad. Sci. USA **113**, 2904 (2016).

[24] Y. Qi, W. Shi, P. G. Naumov, N. Kumar, W. Schnelle, O. Barkalov, C. Shekhar, H. Borrmann, C. Felser, B. Yan, and S. A. Medvedev, Pressure-driven superc- onductivity in the transition-metal pentatelluride $HfTe_5$, Phys. Rev. B **94**, 054517 (2016).

[25] Z. Fan, Q. F. Liang, Y. B. Chen, S. H. Yao, and J. Zhou, Transition between strong and weak topological insulator in $ZrTe_5$ and $HfTe_5$, Sci. Rep. **7**, 45667 (2017).

[26] D. Santos-Cottin, M. Padlewski, E. Martino, S. Ben David, F. Le Mardelé, F. Capitani, F. Borondics, M. D. Bachmann, C. Putzke *et al.*, Probing intraband excitations in $ZrTe_5$: A high-pressure infrared and transport study, Phys. Rev. B **101**, 125205 (2020).

[27] J. L. Zhang, C. Y. Guo, X. D. Zhu, L. Ma, G. L. Zheng, Y. Q. Wang, L. Pi, Y. Chen, H. Q. Yuan, and M. L. Tian, Disruption of the Accidental Dirac Semimetal State in $ZrTe_5$ under Hydrostatic Pressure, Phys. Rev. Lett. **118**, 206601 (2017).

[28] J. L. Zhang, S. J. Zhang, H. M. Weng, W. Zhang, L. X. Yang, Q. Q. Liu, S. M. Feng, X. C. Wang, R. C. Yu, L. Z. Cao *et al.*, Pressure-induced superconductivity in topological parent compound Bi_2Te_3, Proc. Natl. Acad. Sci. USA **108**, 24 (2011).

[29] M. K. Jacobsen, S. V. Sinogeikin, R. S. Kumar, and A. L. Cornelius, High pressure transport characteristics of Bi_2Te_3, Sb_2Te_3, and $BiSbTe_3$, J. Phys. Chem. Solids **73**, 1154 (2012).

[30] N. Su, B. C. Qin, K. J. Zhu, Z. Y. Liu, P. Shahi, J. P. Sun, B. S. Wang, Y. Sui, Y. G. Shi, L. D. Zhao, and J.-G. Cheng, Pressure-induced enhancement of thermoelectric power factor in pristine and hole-doped SnSe crystals, RSC Adv. **9**, 26831 (2019).

[31] K. Lin, Q. Li, R. Yu, J. Chen, J. P. Attfield, and X. Xing, Chemical pressure in functional materials, Chem. Soc. Rev. **51**, 5351 (2022).

[32] R. Wu, J.-Z. Ma, S.-M. Nie, L.-X. Zhao, J.-X. Yin X.Huang, B.-B. Fu, P. Richard, G.- F. Chen, Z. Fang *et al.*, Evidence for topological edge states in a large energy gap near the step edges on the surface of $ZrTe_5$, Phys. Rev. X **6**, 021017 (2016).

[33] H. Wang, C.-K. Li, H. Liu,J. Yan, J. Wang, J. Liu, Z. Lin, . Li, Y. Wang, L. Li, D. Mandrus, X. C. Xie, J. Feng, and J. Wang, Chiral anomaly and ultrahigh mobility in crystalline $HfTe_5$, Phys. Rev. B **93**, 165127 (2016).

[34] P. Giannozzi, O. Andreussi, T. Brumme, O. Bunau, M. Buongiorno Nardelli, M. Calandra, R. Car, C. Cavazzoni, D. Ceresoli, M. Cococcioni, N. Colonna, I. Carnimeo, A. Dal Corso, S. de Gironcoli *et al.*, Advanced capabilities for materials modelling with Quantum ESPRESSO, J. Phys. Condens. Matter **29**, 465901 (2017).

[35] J. P. Perdew, K. Burke, and M. Ernzerhof, Generalized gradient approximation made simple, Phys. Rev. Lett. **77**, 3865 (1996).

[36] S. Grimme, J. Antony, S. Ehrlich, and H. Krieg, A consistent and accurate ab initio parametrization of density functional dispersion correction (DFT-D) for the 94 elements H-Pu, J. Chem. Phys. **132**, 154104 (2010).

[37] D. R. Hamann, Optimized norm-conserving Vanderbilt pseudopotentials, Phys. Rev. B **88**, 85117 (2013).

[38] C. M. Wang, H. Z. Lu, and S. Q. Shen, Anomalous phase shift of quantum oscillations in 3D topological semimetals, Phys. Rev. Lett. **117**, 077201 (2016).

[39] H. Murakawa, M. S. Bahramy, M. Tokunaga, Y. Kohama, C. Bell, Y. Kaneko, N. Nagaosa, H. Y. Hwang, and Y. Tokura, Detection of Berry's phase in a bulk rashba semiconductor, Science **342**, 1490 (2013).

[40] W. Wang, X. Zhang, H. Xu, Y. Zhao, W. Zou, L. He, and Y. Xu, Evidence for layered quantized transport in dirac semimetal $ZrTe_5$, Sci. Rep. **8**, 5125 (2018).

[41] X. Yuan, C. Zhang, Y. Liu, A. Narayan, C. Song, S. Shen, X. Sui, J. Xu, H. Yu, Z. An, J. Zhao, S. Sanvito, H. Yan, and F. Xiu, Observation of quasi-two-dimensional dirac fermions in $ZrTe_5$, NPG Asia Mater. **8**, e325 (2016).

[42] Y. Liu, X. Yuan, C. Zhang, Z. Jin, A. Narayan, C. Luo, Z. Chen, L. Yang, J. Zou, X. Wu, S. Sanvito, Z. Xia, L. Li, Z. Wang, and F. Xiu, Zeeman splitting and dynamical mass generation in Dirac semimetal $ZrTe_5$, Nat. Commun. **7**, 12516 (2016).

[43] G. Zheng, X. Zhu, Y. Liu, J. Lu, W. Ning, H. Zhang, W. Gao, Y. Han, J. Yang, H. Du, K. Yang, Y. Zhang, and M. Tian, Field-induced topological phase transition from a three-dimensional Weyl semimetal to a two-dimensional massive Dirac metal in $ZrTe_5$, Phys. Rev. B **96**, 121401 (2017).

[44] K. Akiba, A. Miyake, Y. Akahama, K. Matsubayashi, Y. Uwatoko, and M. Tokunaga, Phys. Rev. B **95**, 115126 (2017).

[45] Y. Yuan, W. Wang, Y. Zhou, X. Chen, C. Gu, C. An, Y. Zhou, B. Zhang, C. Chen, R. Zhang, and Z. Yang, Pressure-induced superconductivity in topological semimetal candidate $TaTe_4$, Adv. Electron. Mater. **6**, 1901260 (2020).

[46] Y. Liu, Y. J. Long, S. M. Nie, S. J. Zhang, Y. X. Weng, M. L. Jin, W. M. Li, Q. Q. Liu, Y. W. Long, R. C. Yu *et al.*,

Superconductivity in $HfTe_5$ across weak to strong topological insulator transition induced via pressures, Sci. Rep. **7**, 44367 (2017).

[47] P. Sun, B. Wei, J. Zhang, J. M. Tomczak, A. M. Strydom, M. Søndergaard, B. B. Iversen, and F. Steglich, Large Seebeck effect by charge-mobility engineering, Nat. Commun. **6**, 7475 (2015).

[48] Y. Pei, H. Wang, and G. J. Snyder, Band Engineering of Thermoelectric Materials, Adv. Mater. **24**, 6125 (2012).

[49] Q. Zhang, Q. Song, X. Wang, J. Sun, Q. Zhu, K. Dahal, X. Lin, F. Cao, J. Zhou, S. Chen, G. Chen, J. Mao, and Z. Ren, Deep defect level engineering: A strategy of optimizing the carrier concentration for high thermoelectric performance, Energy Environ. Sci. **11**, 933 (2018).

[50] J. Zhu, C. Lee, F. Mahmood, T. Suzuki, S. Fang, N. Gedik, and J. G. Checkelsky, Comprehensive study of band structure driven thermoelectric response of $ZrTe_5$, Phys. Rev. B **106**, 115105 (2022).

[51] J. N. Fuchs, F. Piéchon, and G. Montambaux, Landau levels, response functions and magnetic oscillations from a generalized Onsager relation, SciPost Phys. **4**, 024 (2018).

[52] J. G. Analytis, R. D. McDonald, S. C. Riggs, J. H. Chu, G. S. Boebinger, and I. R. Fisher, Two-dimensional surface state in the quantum limit of a topological insulator, Nat. Phys. **6**, 960 (2010).

[53] C. Brüne, C. X. Liu, E. G. Novik, E. M. Hankiewicz, H. Buhmann, Y. L. Chen, X. L. Qi, Z. X. Shen, S. C. Zhang, and L. W. Molenkamp, Quantum Hall effect from the topological surface states of strained bulk HgTe, Phys. Rev. Lett. **106**, 126803 (2011).

[54] K. Shrestha, V. Marinova, B. Lorenz, and P. C. W. Chu, Shubnikov-de Haas oscillations from topological surface states of metallic $Bi_2Se_{2.1}Te_{0.9}$, Phys. Rev. B **90**, 241111 (2014).

[55] A. A. Taskin and Y. Ando, Berry phase of nonideal Dirac fermions in topological insulators, Phys. Rev. B **84**, 035301 (2011).